

Kinematics of SDSS subdwarfs: Structure and substructure of the Milky Way halo

M.C. Smith^{1*}, N.W. Evans¹, V. Belokurov¹, P.C. Hewett¹, D.M. Bramich², G. Gilmore¹, M.J. Irwin¹, S. Vidrih^{1,3,4}, D.B. Zucker^{1,5,6}

¹*Institute of Astronomy, University of Cambridge, Madingley Road, Cambridge, CB3 0HA, UK*

²*Isaac Newton Group of Telescopes, Apartado de Correos 321, E-38700 Santa Cruz de la Palma, Canary Islands, Spain*

³*Astronomisches Rechen-Institut, Zentrum für Astronomie der Universität Heidelberg, Mönchhofstrasse 12-14, 69120 Heidelberg, Germany*

⁴*Faculty of Mathematics and Physics, University of Ljubljana, Ljubljana, Slovenia*

⁵*Department of Physics, Macquarie University, North Ryde, NSW 2109, Australia*

⁶*Anglo-Australian Observatory, P. O. Box 296, Epping, NSW 1710, Australia*

AcceptedReceived;in original form

ABSTRACT

We construct a new sample of ~ 1700 solar neighbourhood halo subdwarfs from the Sloan Digital Sky Survey, selected using a reduced proper motion diagram. Radial velocities come from the SDSS spectra and proper motions from the light-motion curve catalogue of Bramich et al. (2008). Using a photometric parallax relation to estimate distances gives us the full phase-space coordinates. Typical velocity errors are in the range $30 - 50 \text{ km s}^{-1}$. This halo sample is one of the largest constructed to-date and the disc contamination is at a level of $\lesssim 1$ per cent. This enables us to calculate the halo velocity dispersion to excellent accuracy. We find that the velocity dispersion tensor is aligned in spherical polar coordinates and that $(\sigma_r, \sigma_\phi, \sigma_\theta) = (143 \pm 2, 82 \pm 2, 77 \pm 2) \text{ km s}^{-1}$. The stellar halo exhibits no net rotation, although the distribution of v_ϕ shows tentative evidence for asymmetry. The kinematics are consistent with a mildly flattened stellar density falling with distance like $r^{-3.75}$.

Using the full phase-space coordinates, we look for signs of kinematic substructure in the stellar halo. We find evidence for four discrete overdensities localised in angular momentum and suggest that they may be possible accretion remnants. The most prominent is the solar neighbourhood stream previously identified by Helmi et al. (1999), but the remaining three are new. One of these overdensities is potentially associated with a group of four globular clusters (NGC5466, NGC6934, M2 and M13) and raises the possibility that these could have been accreted as part of a much larger progenitor.

Key words: Galaxy: kinematics and dynamics – Galaxy: halo – solar neighbourhood stars: subdwarfs – Population II

1 INTRODUCTION

In recent years, there has been an impressive and growing body of evidence that the stellar halo of the Galaxy is composed of the remnants of accretion and merging events. The Sloan Digital Sky Survey (SDSS; York et al. 2000) has made a significant contribution to this field, with a series of major discoveries, including the Monoceros Ring (Newberg et al. 2002; Yanny et al. 2003), the Virgo Overdensity (Jurić et al. 2008) and the Hercules-Aquila Cloud (Belokurov et al. 2007). These structures were identified as overdensities of resolved stars, exploiting the deep and homogeneous photometry in 5 bands (u, g, r, i and z) that SDSS provides in a large area around the North Galactic Cap.

The aim of this paper is to search for substructure in the Galactic halo with SDSS data, but this time using kinematic methods. This technique led to the discovery of the disrupting Sagittarius dwarf galaxy and its Stream, which were found serendipitously in a radial velocity survey of the outer Galactic Bulge (Ibata et al. 1994, 1995). It has also led to the identification of a number of probable halo streams found by spectroscopic surveys of the blue horizontal branch population (e.g., Arnold & Gilmore 1992; Clewley et al. 2005). More rarely, searches for kinematic substructure have exploited both proper motion and radial velocities. For example, high quality proper motions provided by HIPPARCOS, together with ground-based radial velocities, enabled Helmi et al. (1999, hereafter H99) to construct three-dimensional velocity distributions for an almost complete sample of nearby halo stars and to identify a nearby stream as a coherent structure in velocity space.

* msmith@ast.cam.ac.uk

Section	Description of cut	Number of objects
2.1	Initial sample with high quality astrometry	370,000
2.1	Satisfy RPM cut	27,000
2.2	With high quality spectra	2,704
2.3	Colour within range of photometric parallax	2,183
2.3	Distance < 5.0 kpc	1,717

Table 1. The number of subdwarf candidates after the respective cuts.

Samples of accurate proper motions can be obtained through repeated astrometric observations over a significant temporal baseline. Most of the SDSS data has limited variability information, with one important exception: during the three months when the Southern Galactic Cap is available for observation, SDSS repeatedly scanned a ~ 290 square degree area – known as Stripe 82 – to detect supernovae (see e.g., Abazajian et al. 2009).

Bramich et al. (2008) have presented a Stripe 82 catalogue of almost 4 million “light-motion curves”, in which objects are matched between the ~ 30 epochs, taking into account the effects of any proper motion over the eight-year baseline. The catalogue is complete down to a magnitude 21.5 in u, g, r and i , and to magnitude 20.5 in z . Each object has its proper motion calculated based only on the multi-epoch SDSS J2000 astrometric measurements. It reaches almost 2 magnitudes fainter than the SDSS/USNOB catalogue (Monet et al. 2003; Munn et al. 2004), making it the deepest large-area photometric and astrometric catalogue available.

Substructure in the catalogue of Bramich et al. (2008) has already been identified by looking for overdensities. For example, Watkins et al. (2009) isolated the RR Lyrae variables by a combination of colour, metallicity and period cuts. The Hercules-Aquila Cloud and the Sagittarius Stream were both clearly identifiable in the Stripe 82 RR Lyrae population, together with a completely new and distant substructure called the Pisces Overdensity. Thus far, however, searches for kinematic substructure in the Stripe 82 data have not been carried out, and the object of this paper is to remedy this deficiency.

In Section 2, we show how to isolate a sample of nearby halo subdwarfs from the catalogue of Bramich et al. (2008). The kinematic properties of the local halo subdwarf population are discussed in Section 3. We develop algorithms to search for kinematic substructure, recovering the known H99 stream in Section 4, as well as new kinematic overdensities in Section 5.

2 THE SUBDWARF SAMPLE

2.1 Reduced proper motion (RPM) diagram

The full Bramich et al. (2008) catalogue contains proper motions, μ , for ~ 1 million stars down to magnitudes of $r \sim 21.5$. We trim this sample by enforcing the following three conditions to retain only those objects with high quality data. First, we insist that the mean object type ≥ 5.7 . This requires an object to be classified as a star in ≥ 90 per cent of epochs. This is less than 100 per cent in order to retain objects that have been misclassified in a limited number of epochs due to problems with the SDSS star-galaxy separation algorithm. In the Bramich et al. (2008) catalogue, this occurs particularly in the final season, when observations were not exclusively taken in photometric conditions. Secondly, we insist that the proper-motion error is less than 4 mas yr^{-1} to remove stars with poorly determined proper motions. All of our final sample have

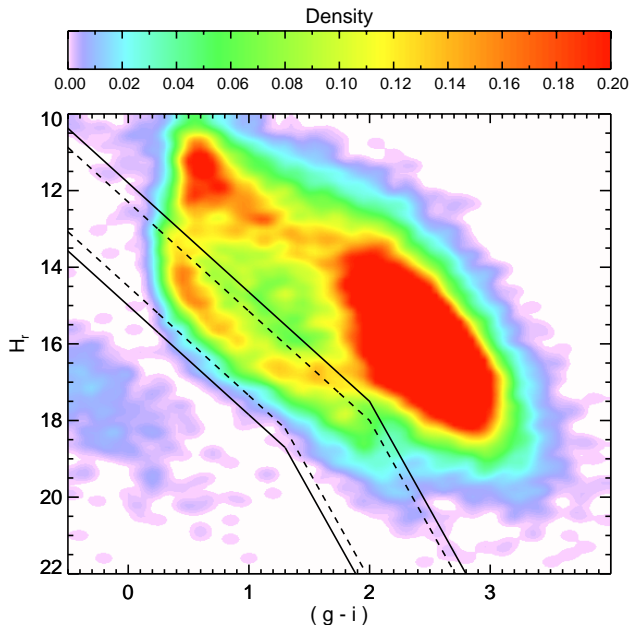


Figure 1. Reduced proper motion diagram for the Bramich et al. (2008) sample. The solid lines denote the approximate boundary of the subdwarf population. The dashed lines denote the stricter boundary employed to reduce contamination from disc main-sequence dwarfs (which lie to the upper-right of the boundary) or white dwarfs (which lie to the lower-left). To aid clarity in this figure, we have imposed an additional proper motion cut ($\mu > 30 \text{ mas yr}^{-1}$); however, no such cut was applied to our sample. Note that the colour-scale saturates at 20 per cent of the peak density.

proper motions based on at least 23 epochs and time-baselines of over 4 years, which indicates that the formal proper motion errors should be reliable. Thirdly, we impose $r < 19.5$ to reduce contaminants (see Appendix A for more details). Here, and elsewhere in the paper, all magnitudes are corrected for extinction using the maps of Schlegel et al. (1998). The magnitude cut is often redundant as we also later require stars to have SDSS spectra, and there are very few spectra for stars fainter than this limit.

We select our candidate subdwarfs from a reduced proper motion (RPM) diagram. The r -band RPM is given by

$$H_r = r + 5 \log \frac{\mu}{\text{mas yr}^{-1}} - 10, \quad (1)$$

where μ is the proper-motion and r is the apparent magnitude. This uses a star’s proper motion as a proxy for distance, allowing us to separate cleanly populations with different absolute magnitudes (e.g. main sequence dwarfs, white dwarfs, giants). Although disc and halo dwarfs have similar absolute magnitudes, they have very different kinematics. As a consequence, the faster moving halo stars appear offset from the dominant disc stars in the RPM diagram, which can be seen clearly in our data (Fig 1).

Note that for the purposes of this figure, we have enforced an additional cut that $\mu > 30 \text{ mas yr}^{-1}$ to emphasise the distinction between disc and halo dwarfs. As we relax this criterion, the diagram becomes populated by slower moving halo dwarfs which lie in the boundary region between the two populations on this RPM diagram. Slower moving disc dwarfs, on the other hand, lie in the upper portion of the diagram well away from our cuts and hence do not contaminate our final sample. Therefore, although placing such a cut on the magnitude of μ aids the clarity of this figure, it is not necessary for our final sample. By not placing a cut on μ , we

make the process of quantifying the kinematic bias much easier (as described later in Section 2.4).

We now define our halo subdwarf region as

$$\begin{aligned} H < 2.85(g-i) + 11.8 & \text{ for } (g-i) \leq 2 \\ H < 5.63(g-i) + 6.24 & \text{ for } (g-i) > 2 \\ H > 2.85(g-i) + 15.0 & \text{ for } (g-i) \leq 1.3 \\ H > 5.63(g-i) + 11.386 & \text{ for } (g-i) > 1.3. \end{aligned} \quad (2)$$

To construct as clean a sample as possible, we reject all objects that lie within $\Delta H = 0.5$ of the boundary, resulting in the final region shown by the dashed line in Fig. 1.

2.2 SDSS spectra

As well as its photometric survey, the 7th SDSS Data Release (DR7; Abazajian et al. 2009) also has a large number of spectra. These are predominantly of galaxies and quasars, but also include stellar targets (Yanny et al. 2009). These have been analysed by a pipeline designed to derive the radial velocities and fundamental stellar atmospheric parameters (the SEGUE Spectral Parameter Pipeline, or SSPP; Lee et al. 2008a,b; Allende Prieto et al. 2008). Typical internal errors reported by the pipeline are $\delta v_r \sim 3.8 \text{ km s}^{-1}$ for the radial velocity and $\delta[\text{Fe}/\text{H}] \sim 0.1$ dex for the metallicity. Validation of this pipeline was carried out through comparison with high resolution spectra (Allende Prieto et al. 2008), which showed that the SSPP external errors are approximately 2.4 km s^{-1} in velocity and 0.11 dex in metallicity. To account for this, we add these errors in quadrature to the internal errors from the SSPP.

We have cross-matched our candidate subdwarf sample with the SSPP DR7 catalogue, and found that ~ 7 per cent have suitable spectra – defined as those with SSPP flag set to ‘nnnn’, which indicates that there are no cautionary signs and the stellar parameters should be well determined (Lee et al. 2008a). Additionally, we reject all spectra with radial velocity error greater than 50 km s^{-1} . If there are multiple spectra, we take the spectrum with greatest signal-to-noise ratio. The median errors in our cross-matched sample are $\delta v_r = 4.1 \text{ km s}^{-1}$ and $\delta[\text{Fe}/\text{H}] = 0.12$ dex.

The SDSS spectroscopic target selection function is very heterogeneous, covering a wide variety of targets (Abazajian et al. 2009; Yanny et al. 2009). This will introduce selection effects into our sample, for example much of the stellar targeting is biased towards bluer populations which are likely to have lower metallicities. However, we do not believe that this will introduce any significant kinematic bias. If there was a strong correlation between the kinematics and metallicity *within* the halo subdwarf population, then our results would be kinematically biased. However, as we will see later in Section 3, we do not find any such strong correlation in our sample.

2.3 Distances, metallicities and surface gravities

To obtain distances for our subdwarfs, we use a photometric parallax relation. Such a relation has been established for main-sequence stars in the SDSS photometric system by Ivezić et al. (2008). It was constructed through observations of eleven globular clusters and tested using additional clusters and stars with trigonometric parallax distances.

The relation, which is given in equations (A1-A5) of Ivezić et al. (2008), is valid for dwarfs with $0.2 < g-i < 4$ and incorporates a correction to account for systematic trends with metallicity. According to Ivezić et al. (2008), the intrinsic scatter in this relation

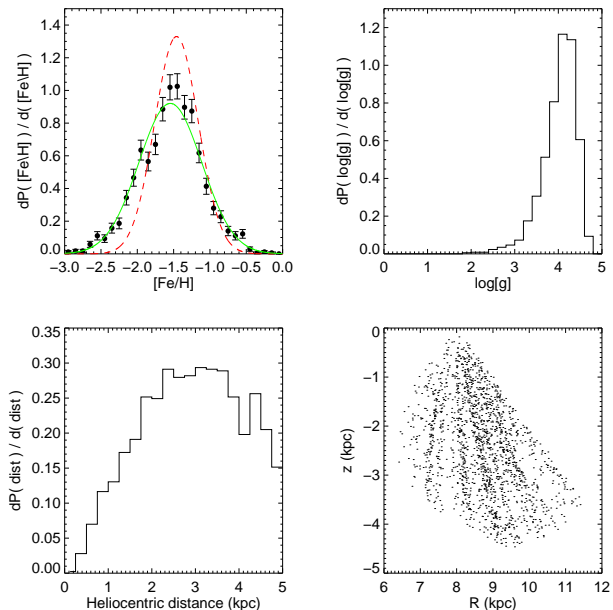


Figure 2. Various properties of our subdwarf sample, namely metallicity (top left), surface gravity (top right), heliocentric distance (bottom left) and spatial distribution in Galactocentric cylindrical coordinates (bottom right). Our $[\text{Fe}/\text{H}]$ distribution may be subject to biases due to the nature of the sample construction (see Section 2.3). For comparison, the dashed curve shows the distribution from Ivezić et al. (2008). The spatial distribution is inhomogeneous due to the fact that the proper motion accuracy, which depends on the number of epochs that a star was observed, varies significantly across our field of view (see Bramich et al. 2008).

is ~ 0.13 mag, which is a lower limit on the true uncertainty. An upper limit of 0.3 has been estimated by Sesar et al. (2008, see also Jurić et al. 2008), who use candidate binary stars to assess the reliability of the photometric parallaxes. Therefore, for this work, we take a fiducial uncertainty of 0.2 mag.

The relation we adopt differs from that of Ivezić et al. (2008) in that we have chosen not to incorporate their turn-off correction (given by equation A6 of their paper). Instead, we have constructed our own correction using the stellar models of Dotter et al. (2008). Our procedure, which is described in Appendix B, results in the following correction for stars with $0.3 < g-i < 0.6$,

$$\Delta M_r = a_0 x + a_1 x y + a_2 x^3 + a_3 x^2 y + a_4 x^3 y, \quad (3)$$

where $x = (g-i) - 0.6$, $y = [\text{Fe}/\text{H}]$, and $a_0 = 2.87$, $a_1 = 2.25$, $a_2 = -9.79$, $a_3 = 2.07$, $a_4 = 0.31$. Due to the scatter in this relation we increase the uncertainties in the distances of the stars in this colour range (see Appendix B).

Using the accurate photometry from the multi-epoch Stripe 82 data (with mean $\delta(g-i) < 0.01$) and taking $[\text{Fe}/\text{H}]$ from the spectra, we now estimate a distance. Combining the uncertainty in the Ivezić et al. (2008) relation with the error on $[\text{Fe}/\text{H}]$, we find that the median distance error in our sample is ~ 11 per cent. Our distances are mostly in the range 0.5 to 5 kpc, although there are a small number of stars further out. However, unless otherwise stated, henceforth we only use stars with heliocentric distance $D < 5$ kpc. Beyond this, the errors on the velocities become too large because of the uncertainty in the proper motion. This gives us a final sample of 1717 halo subdwarfs, as summarized in Table 1.

There are a number of potential sources of contamination in

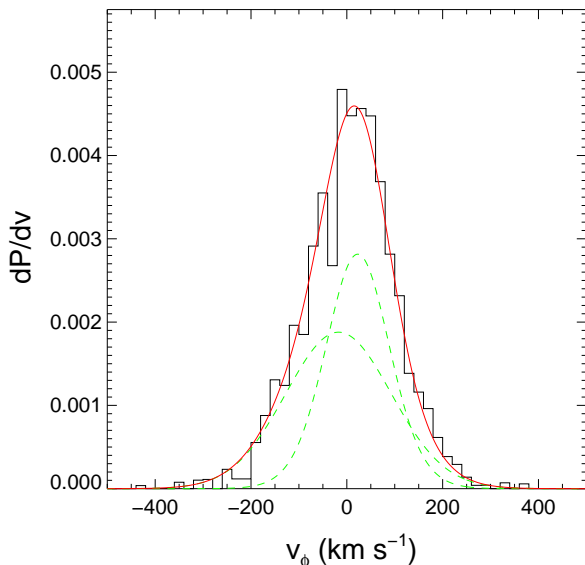


Figure 4. Multi-component Gaussian fit to the v_ϕ velocity distribution. The statistically preferred fit is this two-component model, which is better able to reproduce the asymmetry than the single Gaussian shown in Fig. 3.

the sample, including white dwarfs, thin and thick disc stars and background giants. These are discussed in turn in Appendix A, which concludes that the actual level of contamination is very small ($\lesssim 1$ per cent). As a check that our sample is clean, we examine various non-kinematic properties in Fig. 2. We can immediately see that the surface gravities are consistent with that of a dwarf population. Although there are a handful of stars with low gravity, the vast majority have $\log(g) > 3$. These outliers are most likely caused by misestimation of $\log(g)$ from the spectra. The median error on $\log(g)$ for our sample is 0.25 dex, but the median error for those stars with $\log(g) < 3$ is 0.5 dex.

The distribution of $[\text{Fe}/\text{H}]$ is also consistent with a halo sample. In Fig. 2, we show the observed distribution along with the Gaussian found by Ivezić et al. (2008) using photometric metallicities. Although the mean of our distribution ($[\text{Fe}/\text{H}] = -1.55$) is similar to theirs ($[\text{Fe}/\text{H}] = -1.46$), it is clear that our distribution is significantly broader (with a dispersion 0.43 as opposed to 0.3). This broadening and offset is most likely due to the underlying selection function for the SEGUE spectra, which will clearly have a significant effect on the $[\text{Fe}/\text{H}]$ distribution.

2.4 Kinematic bias

One problem with our sample is that it suffers from kinematical bias. This is caused by the cut on H_r , which selects stars via their tangential velocity, rather than their proper motion. Using a cut on H_r , instead of the proper motion, makes the task of quantifying the bias significantly easier, since assumptions about the underlying distance distribution (i.e., luminosity function) are not needed.

We calculate our detection efficiency as follows. For each sub-dwarf in our final sample, we take the sky coordinates and create a mock sample of 50,000 fake stars. Then, for each mock star, we select M_r and $g-i$ at random from our observed distribution. Note that for each realization *both* the magnitude and color are assigned from one star. We then fix the kinematics by choosing velocities

from Gaussians with the halo velocity dispersions from Képley et al. (2007) and no net motion (following Allende Prieto et al. 2006). We determine the tangential component of the velocity (v_{tan}) with respect to the line-of-sight between the Sun and the mock star.¹ Given this information we can calculate the reduced proper motion using,

$$H_r = M_r + 5 \log_{10} \left(\frac{v_{\text{tan}}}{4.74 \text{ km s}^{-1}} \right). \quad (4)$$

The efficiency is then given by the fraction of mock stars which pass our reduced proper motion cut.

3 GLOBAL KINEMATIC PROPERTIES

3.1 Data

Here, we calculate properties of the first and second moments of the halo velocity distribution. We begin by defining our coordinate systems. We take the solar radius as 8 kpc, the velocity of the local standard of rest as 220 km s^{-1} and the solar peculiar velocity as given by Dehnen & Binney (1998). The Galactocentric Cartesian reference frame is denoted by (x, y, z) , where the axes are oriented along the line connecting the Sun and the Galactic centre, in the direction of disc rotation and toward the North Galactic Pole, respectively. This is a right handed frame so that the Sun is at $x = -8.0$ kpc. Velocity components resolved with respect to this coordinate system are (v_x, v_y, v_z) .

We also use cylindrical and spherical polar coordinates defined with respect to a right-handed Galactocentric frame. Cylindrical polars are denoted by (R, ϕ, z) where R is radially outward, ϕ is positive in the direction of counter-rotation of the disc and z is positive towards the North Galactic Pole. The corresponding velocity components are (v_R, v_ϕ, v_z) . Similarly, spherical polars are denoted (r, θ, ϕ) where r is radially outward and θ is increasing towards the South Galactic Pole. The velocity components are (v_r, v_ϕ, v_θ) . So, for stars in the solar neighbourhood, $v_\theta \approx -v_z$. Note that disc stars rotate with $v_\phi \approx -220 \text{ km s}^{-1}$, which is a consequence of adopting a right-handed system.

The values for the mean and dispersion of the velocity components in spherical and cylindrical polars are given in Table 2. They are calculated using a maximum likelihood technique which corrects for the spread that results from observational errors, namely,

$$L(\mu_i, \sigma_i) = \prod_{k=1}^N \left\{ \frac{1}{\sqrt{2\pi(\sigma_i^2 + \delta v_{i,k}^2)}} \exp \left[\frac{-(v_{i,k} - \mu_i)^2}{2(\sigma_i^2 + \delta v_{i,k}^2)} \right] \right\}^{(1/\epsilon_k)} \quad (5)$$

where μ_i and σ_i are the mean and dispersion of velocity component i , whilst $v_{i,k}$ and $\delta v_{i,k}$ are the velocity and its uncertainty for the k th star, ϵ_k is the detection efficiency for this star, and N is the total number of stars in the sample. The errors on the individual velocities are calculated using Monte Carlo methods, incorporating the errors on the proper motion, distance and radial velocity. The median error in (v_r, v_ϕ, v_θ) is $(38, 47, 35) \text{ km s}^{-1}$. The magnitude of the errors differs between the three components because of the location of our field, which causes the proper motion to contribute

¹ To calculate v_{tan} requires us to assign a distance to each mock star, which we do at random from the observed distribution. This means that the efficiency does have a dependence on the distance distribution; however this dependence is negligible since equation (4) is a function of the tangential velocity rather than the proper motion.

System	Component	$\langle v \rangle$ (km s ⁻¹)	σ_v (km s ⁻¹)
Spherical	v_r	$8.9^{+2.8}_{-2.6}$	$142.7^{+2.0}_{-1.7}$
	v_ϕ	$2.3^{+1.6}_{-1.8}$	82.4 ± 1.4
	v_θ	$2.4^{+1.6}_{-1.4}$	77.3 ± 1.1
Cylindrical	v_R	8.9 ± 2.6	$138.2^{+2.0}_{-1.7}$
	v_z	-1.2 ± 1.6	$89.3^{+1.3}_{-1.1}$

Table 2. Efficiency weighted mean velocities and their dispersions for our halo sample in both spherical and cylindrical polar coordinates. The values are obtained using a standard maximum likelihood technique which incorporates the spread that results from observational errors (see equation 5). The cross-terms or covariances are reported in a separate paper (Smith, Evans & An 2009).

Reference	System	Component	$\langle v \rangle$ (km s ⁻¹)	σ_v (km s ⁻¹)
Woolley (1978)	Spherical	v_r	–	148
		v_ϕ	–	122
		v_θ	–	82
Norris (1986)	Cartesian	v_x	–	131 ± 6
		v_y	–	106 ± 6
		v_z	–	85 ± 4
Gould & Popowski (1998) (Kinematically selected sample)	Cartesian	v_x	-5 ± 15	171 ± 11
		v_y	9 ± 13	99 ± 8
		v_z	1 ± 8	90 ± 7
Gould & Popowski (1998) (Non-kinematically selected sample)	Cartesian	v_x	-3 ± 9	160 ± 7
		v_y	28 ± 9	109 ± 9
		v_z	2 ± 5	94 ± 5
Chiba & Beers (2000)	Cartesian	v_x	-16 ± 16	141 ± 11
		v_y	26 ± 12	106 ± 9
		v_z	-5 ± 11	94 ± 8
Gould (2003a)	Cartesian	v_x	-1 ± 3	171 ± 10
		v_y	9 (fixed)	99 ± 8
		v_z	2 ± 3	90 ± 7
Kepley et al. (2007)	Cylindrical	v_R	-4 ± 11	157 ± 8
		v_ϕ	-23 ± 8	110 ± 6
		v_z	-1 ± 6	84 ± 4

Table 3. Some determinations of the halo velocity parameters from the literature. Note that v_ϕ is defined counter to the direction of disc rotation and for nearby samples $v_\phi \approx -v_y$. With the exception of Kepley et al. (2007), the estimates for the bulk motion have been standardised using the value of the solar motion from Dehnen & Binney (1998). Kepley et al. (2007) use the value from Mihalas & Binney (1981) and as a consequence their estimate of $\langle v_\phi \rangle$ is subject to an offset of ~ 7 km s⁻¹.

Component	Corr[v_i, v_j]	$\alpha_{i,j}$ (°)
[v_r, v_θ]	0.052 ± 0.028	2.2 ± 1.2
[v_r, v_ϕ]	-0.019 ± 0.042	-1.6 ± 3.6
[v_ϕ, v_θ]	-0.073 ± 0.050	-36.7 ± 24.1

Table 4. Efficiency weighted correlation coefficients and tilt angles for halo stars with $|z| > 1$ kpc (see Smith, Evans & An 2009, for the definitions of these quantities). Note that these values are not identical to those quoted in Smith, Evans & An (2009) because the ones given here incorporate our new turn-off correction for the photometric parallax relation (see equation 3). However, the difference is small and none of the conclusions of Smith, Evans & An (2009) are affected.

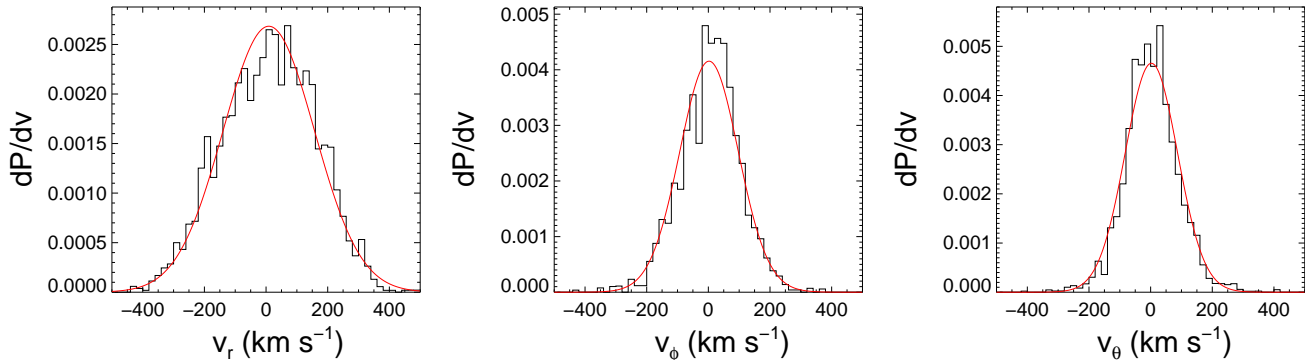


Figure 3. The velocity distributions of the halo subdwarf sample. The velocity components are resolved in spherical polar coordinates with prograde rotation corresponding to $v_\phi < 0$. The solid curves show Gaussian fits to the data, with the corresponding parameters given in Table 2.

more to the v_ϕ component. Furthermore, because the uncertainties are larger in the tangential direction the errors are correlated, with the orientation of the error ellipse varying along the field.

The maximum likelihood velocity distributions are displayed in Fig. 3. Although the Gaussian models provide a reasonable match to the observations for v_r and v_θ , it appears that v_ϕ exhibits some asymmetry. Accordingly, we repeated the maximum likelihood fitting allowing for multiple Gaussian components. We determine whether a multiple Gaussian model is statistically preferred by comparing the ratio of likelihoods, where $-2 \ln(L_i/L_{i+1}) > 3$ indicates that a model with $(i + 1)$ components is preferred. The value of 3 comes from the fact that there are three additional parameters in the model with $(i + 1)$ components.

Although for v_r there is only a marginal improvement with multiple Gaussians, for v_θ a two-component fit is clearly preferred, reflecting the fact that the distribution is narrower than a single Gaussian yet has noticeable wings for $|v_\theta| \gtrsim 200 \text{ km s}^{-1}$. As a consequence, this two-component model has one main narrow component (with $\sigma = 64 \text{ km s}^{-1}$) and a shallow broad component (with $\sigma = 135 \text{ km s}^{-1}$), both of which have mean close to 0 km s^{-1} . The presence of these wings can be understood when one considers the substructures present in our sample (which will be discussed later).

For v_ϕ , a two-component fit is also preferred, with approximately equal contributions from the two components with dispersions of 48.1 and 98.9 km s^{-1} and means 22.8 and -17.1 km s^{-1} , respectively (see Fig. 4). This provides a better match to the asymmetry in the v_ϕ distribution. We believe that this asymmetry is not caused by problems with our efficiency correction nor with contamination from the disc (see Appendix A). This leads us to conclude that it is a real effect. It appears that the asymmetry is more pronounced for metal-rich stars ($[\text{Fe}/\text{H}] > -1.5$ dex), although we find no evidence for dramatic trends with metallicity, such as those postulated by Morrison et al. (2009). Neither do we see any clear gradient in $\langle v_\phi \rangle$ as a function of height from the Galactic plane. Although we identify various kinematic substructures in our sample (see Sections 4 and 5), none of these can explain this asymmetry.

In Table 3, we present earlier determinations of the mean velocity and dispersion for halo stars in the literature. Our dispersions are significantly smaller than previous estimates (such as Gould & Popowski 1998; Chiba & Beers 2000; Gould 2003a; Kępley et al. 2007), although the ratios are in approximate agreement. Comparison between different investigations is clouded by the fact that some of the earlier samples are subject to significant levels of disc contamination. Also, it is not always clear whether corrections have

been made for the spread induced by measurement errors. The dispersions estimated by Gould (2003a) are upper limits as they do not incorporate the spread due to uncertainties in their photometric parallax relation.

There has also been controversy in the literature with regards to the mean rotational velocity of the halo, with estimates of prograde (Chiba & Beers 2000; Kępley et al. 2007), no rotation (Gould & Popowski 1998; Allende Prieto et al. 2006), or retrograde (Majewski 1992). Our value of $\langle v_\phi \rangle = 2.3^{+1.6}_{-1.8} \text{ km s}^{-1}$ is approximately consistent with a non-rotating halo. Since our kinematic selection is biased against stars with $v_\phi \approx -200 \text{ km s}^{-1}$, we might expect that our estimate of $\langle v_\phi \rangle$ is dependent on the efficiency correction. However, tests show that this is not the case. Our calculation in Section 2.4 requires an assumption for the rotational velocity of the halo, but if we adopt values anywhere between -20 and 20 km s^{-1} , then our measured value of $\langle v_\phi \rangle$ varies by less than 1 km s^{-1} . However, it is still true that our estimate of $\langle v_\phi \rangle$ (as with any of the estimates from Table 3) is degenerate with the assumed value for the local standard of rest (220 km s^{-1}).

Another result of interest is the value of $\langle v_r \rangle$, which is 3σ away from zero. It is not clear why we obtain a positive value of $\langle v_r \rangle$ (i.e., radially outward). There are a variety of potential issues that could cause this effect: kinematic substructure; systematic errors in the velocities (either the radial velocities or proper motions) or distances; the presence of binary stars, for which we would systematically underestimate their distances; bias in the determination of the solar motion with respect to the local standard of rest. We do not investigate this issue further in the present paper.

We also calculate the efficiency weighted correlation coefficients and tilt angles, as defined in Smith, Evans & An (2009), for the 1,568 stars with $|z| > 1 \text{ kpc}$. Although the data used here is the same as that of Smith, Evans & An (2009), our sample differs in that we are now incorporating our new turn-off correction to the parallax relation (see equation 3 and Appendix B). The values are given in Table 4. These are very similar to those quoted in Smith, Evans & An (2009) and their conclusions are not affected by this new parallax correction term.

3.2 Modelling

Taking our cue from the recent arguments of Fellhauer et al. (2006), let us assume that the gravitational potential of the dark halo is spherically symmetric. If the halo has a flat rotation curve of amplitude $v_0 (= 220 \text{ km s}^{-1})$, then the potential is

$$\psi = -v_0^2 \log r. \quad (6)$$

We now seek a phase space distribution function for the stellar halo that can reproduce the observed kinematics of the SDSS subwarfs. From Jeans Theorem (see, e.g., Binney & Tremaine 1987), the distribution function must depend on the integrals of motion, namely the binding energy E , the components of angular momentum, J_x , J_y , J_z , together with the total angular momentum, J .

A number of authors (White 1985; de Zeeuw et al. 1996) have shown that the stellar density laws of the form

$$\rho = \rho_0 r^{-\gamma} \sin^{2n} \theta \quad (7)$$

can be reproduced by distribution functions

$$f_{m,n}(E, J^2, J_z^2) = \eta_{m,n} J^{2m} J_z^{2n} \exp[(\gamma + 2n + 2m)E], \quad (8)$$

where $m+n > -1$ and $2n > -1$, and $\eta_{m,n}$ is a normalization constant (given in equation 3.5 of de Zeeuw et al. 1996). Note that we have written m and n so that our notation is consistent with earlier work, but m and n are not necessarily integers.

The corresponding velocity second moments are

$$\begin{aligned} \rho \langle v_r^2 \rangle &= \frac{\rho_0 v_0^2}{2m + 2n + \gamma} \frac{\sin^{2n} \theta}{r^\gamma}, \\ \rho \langle v_\theta^2 \rangle &= \frac{m + n + 1}{n + 1} \rho \langle v_r^2 \rangle, \\ \rho \langle v_\phi^2 \rangle &= (2n + 1) \rho \langle v_\theta^2 \rangle. \end{aligned} \quad (9)$$

So, for example, if $m = n = 0$, the model is isotropic and all three velocity dispersions are just $v_0 / \sqrt{3}$. This is a well-known result for isothermal populations. More generally, for fixed γ and n , the velocity dispersions and the density have the same angular dependence for all m , but the anisotropy ratios $\langle v_\theta^2 \rangle / \langle v_r^2 \rangle$ and $\langle v_\phi^2 \rangle / \langle v_r^2 \rangle$ do depend on m .

A flexible way to model the stellar halo is to build further distribution functions by linear superposition. Here, our aim is to construct a simple distribution function that reproduces the kinematics of the SDSS subwarfs, and so we choose

$$f(E, J^2, J_z^2) = \alpha_{m,0} f_{m,0} + \alpha_{m,1} f_{m,1}, \quad (10)$$

where the $\alpha_{m,n}$ are constants specifying the fraction contributed by each component. The corresponding density law is flattened and has the form

$$\rho(r, \theta) = \rho_0 r^{-\gamma} + \rho_1 r^{-\gamma} \sin^2 \theta. \quad (11)$$

We require that at $R = 8.70$ kpc and $z = -2.41$ kpc (the centroid of our SDSS subdwarf population)

$$\langle v_r^2 \rangle^{1/2} = 143 \text{ km s}^{-1}, \quad \langle v_\theta^2 \rangle^{1/2} = 77 \text{ km s}^{-1}, \quad \langle v_\phi^2 \rangle^{1/2} = 82 \text{ km s}^{-1}. \quad (12)$$

The advantage of a two component model (10) is that there is a unique solution. There are three velocity dispersion constraints, and there are three unknowns, namely the radial fall-off γ , the index m and the ratio ρ_1/ρ_0 (or equivalently $\alpha_{m,1}/\alpha_{m,0}$). Solving the non-linear simultaneous equations numerically gives the solution $\gamma = 3.75$, $m = -0.72$ and $\rho_1/\rho_0 = 0.063$.

In other words, the SDSS subdwarf kinematics are consistent with a stellar halo in which the density falls off like $r^{-3.75}$, somewhat steeper than the $r^{-3.5}$ advocated in the classical work on the metal-poor populations of the halo (e.g., Freeman 1987). The axis ratio of the stellar distribution can be computed from

$$q = \left[1 + \frac{\rho_1}{\rho_0} \right]^{-1/\gamma} \quad (13)$$

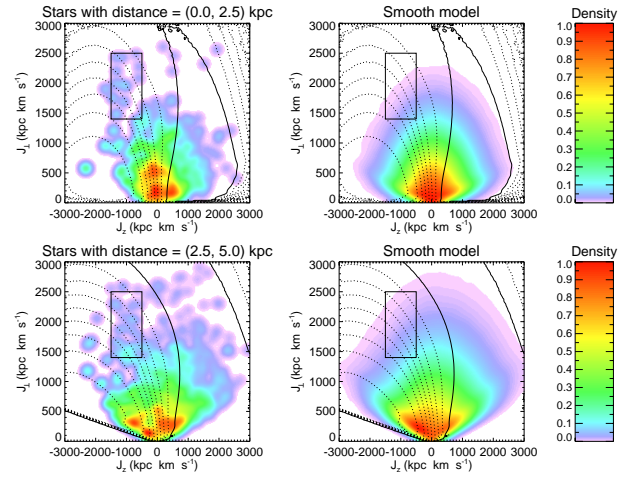


Figure 5. The distribution of angular momentum for our subwarfs (left) and for an artificial smooth halo (right). These plots cover the distance range 0 – 2.5 kpc (top) and 2.5 – 5 kpc (bottom). The contours denote our detection efficiency in steps of 10 per cent, where the solid line corresponds to the 90 per cent contour. The box corresponds to the location of the kinematic stream identified by Helmi et al. (1999). In this coordinate system the Sun would lie at approximately $(-1800, 0)$ kpc km s $^{-1}$.

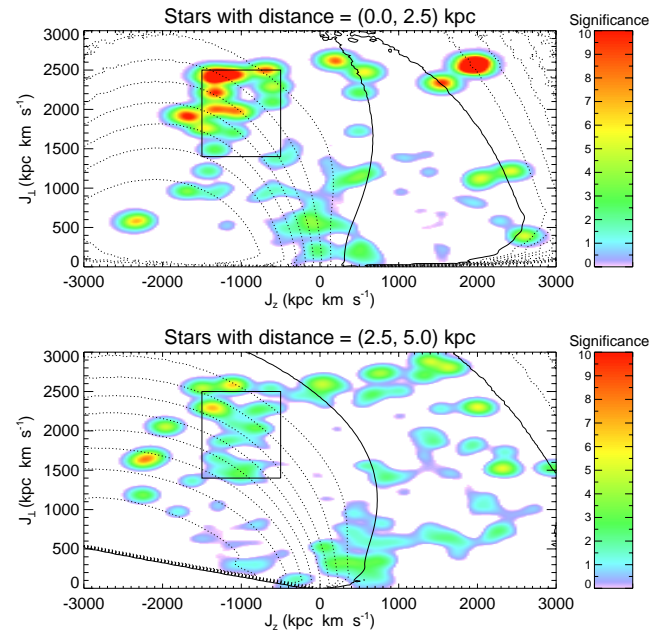


Figure 6. The distribution of angular momentum residuals for subwarfs in the distance range 0 – 2.5 kpc (top) and 2.5 – 5 kpc (bottom). The residuals are obtained after subtracting a smooth model from the observed distribution. The contours and H99 boxes are as in Fig. 5. In this coordinate system the Sun would lie at approximately $(-1800, 0)$ kpc km s $^{-1}$.

which gives $q = 0.983$, in other words, very round. This distribution function is not unique, as there are undoubtedly more complicated multi-component models. Nonetheless, it is the simplest distribution function that is consistent with the kinematical data. It is interesting that the triaxial kinematics are consistent with a near-spherical stellar density law.

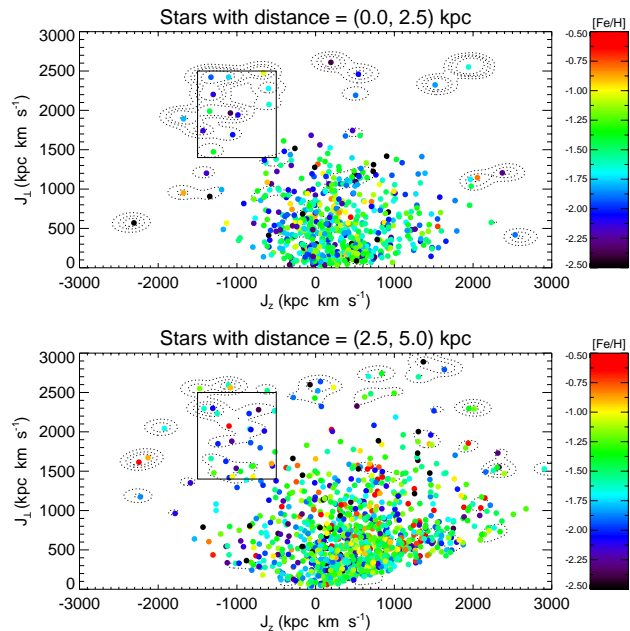


Figure 7. The distribution of the angular momentum components of our subdwarfs in the distance range 0 – 2.5 kpc (top) and 2.5 – 5 kpc (bottom). Stars are colour-coded according to $[\text{Fe}/\text{H}]$ and the colour-range saturates at -2.5 and -0.5 . Contours denote the residuals shown in Fig. 6, corresponding to 1, 3, 5 and 10 sigma significance. There are a number of stars which lie outside the range of this plot; these are given in Table 5. In this coordinate system the Sun would lie at approximately $(-1800, 0)$ kpc km s $^{-1}$.

4 KINEMATIC SUBSTRUCTURE

4.1 Quantification of Substructure

The components of the angular momentum perpendicular and parallel to the symmetry axis of the Galactic plane are

$$J_{\perp} = \left[(y v_z - z v_y)^2 + (z v_x - x v_z)^2 \right]^{1/2}, \quad J_z = x v_y - y v_x. \quad (14)$$

For a solar neighbourhood sample, these two angular momentum components are essentially $J_z \sim -r_{\odot} v_y$ and $J_{\perp} \sim r_{\odot} |v_z|$. Our median errors on (J_z, J_{\perp}) are $(410, 255)$ km 2 s $^{-1}$. If we restrict our sample to the 645 subdwarfs within 2.5 kpc, then the errors are reduced by a factor of ~ 35 per cent. Use of these coordinates is a common approach (e.g. H99, Chiba & Beers 2000), as they are adiabatic invariants in a spherical potential. Note that, unlike H99, we use a right-handed coordinate system, so our values of J_z take an opposite sign to theirs. This means that in our coordinate system the Sun would lie at approximately $(-1800, 0)$ kpc km s $^{-1}$. We weight each star according to the inverse of its detection efficiency to account for kinematic bias and smooth the distribution using a Gaussian kernel with FWHM of $(300, 150)$ kpc km s $^{-1}$, which is the same order of magnitude as the errors. The resulting distribution is plotted in Fig. 5.

To test for substructure, we generate an artificial sample of halo stars using the observed distances and directions of stars in our sample, but generate velocities according to the trivariate Gaussian with means and dispersions given in Table 2. We smooth this distribution and subtract it from the smoothed observed distribution (see Fig. 5). The resulting residual plot is shown in Fig. 6, where the colour-scale shows the significance of overdensities. The significance is quantified by generating a series of efficiency-corrected realisations from our distributions, all of which have the same num-

ber of stars as the observed sample. The scatter in these realisations provides an estimate of $\sigma(J_z, J_{\perp})$, from which we can deduce the significance of our overdensities. We show the overdensities for two distance ranges (the 645 stars with $D < 2.5$ kpc and the 1072 with $2.5 < D < 5$ kpc) and include contours showing the detection efficiency.

Some of the apparent overdensities in the outer regions are artefacts. The smooth model predicts very few stars in the outer regions and hence $\sigma(J_z, J_{\perp})$ is close to zero, which exaggerates the significance of individual outliers. For example, the large clump around $(J_z, J_{\perp}) = (2000, 2500)$ kpc km s $^{-1}$ in the upper panel of Fig. 6 is actually composed of only one star. This can be seen on comparison with Fig. 7, which shows the unbinned (J_z, J_{\perp}) distribution for each of the stars. Note that the figures confirm that our sample is free from significant disc contamination. If there were significant thin or thick disc stars, they would be visible in the region around $-2500 < J_z < -1500$ kpc km s $^{-1}$ and $J_{\perp} < 600$ kpc km s $^{-1}$.

4.2 The H99 Kinematic Stream

The most noticeable feature in Fig. 7 for stars within 2.5 kpc is the asymmetry in J_z for stars with $1500 < J_{\perp} < 2500$ kpc km s $^{-1}$. There is a significant number of stars located around $(J_z, J_{\perp}) \approx (-1000, 2000)$ kpc km s $^{-1}$. This corresponds to the solar neighbourhood kinematic stream first identified by Helmi et al. (1999). They analysed a sample of nearby (i.e. < 1 kpc) halo stars with full six-dimensional phase space information and found that ~ 10 per cent come from a single coherent structure. Subsequently, Képley et al. (2007, hereafter K07) probed a larger volume ($D < 2.5$ kpc) and found a smaller fraction (~ 5 per cent) of stars belonging to this stream. Restricting their sample to 1 kpc, they find a larger fraction (~ 9 per cent) in agreement with H99, although this is not surprising since there is significant overlap between the H99 and K07 samples. Chiba & Beers (2000) also studied an extended version of the H99 halo sample and found a smaller fraction than H99, although the exact percentage is unclear. K07 defined the location of the H99 region as $-1500 < J_z < -500$ and $1400 < J_{\perp} < 2500$, which is indicated in Figs. 5 – 7.

There has also been related work on streams in the solar neighbourhood subdwarfs by Gould (2003b). This analysis, which was based on a large sample of objects with proper motion measurements but without radial velocities or distance determinations, used a Bayesian likelihood analysis to investigate various properties of the nearby subdwarf population. Instead of looking for direct evidence of cold kinematic streams, he quantified the amount of granularity in the velocity space and concluded that no more than 5 per cent of local halo stars (within ~ 300 pc) can come from a single cold stream. Although this number appears to be in conflict with the original results from H99, there is actually no discrepancy as the H99 stream is formed from two separate clumps in velocity space.

The H99 stream is clearly visible in our data, as can be seen in the top panel of Fig. 6, although it appears more diffuse than the detection in K07 (c.f., their fig. 11). Note that this difference cannot be explained by the size of our observational errors, since the median error on (J_z, J_{\perp}) for our H99 stars is $(240, 209)$ km 2 s $^{-1}$. Closer inspection of the upper panel of Fig. 7 shows that the H99 box contains two stars near the centre along with a more diffuse component of 10 stars. These two stars lie almost exactly in the centre of the box at $(J_z, J_{\perp}) \approx (-1035, 1954)$ kpc km s $^{-1}$. The mean metallicity of the two stars is -2.2 dex, which is more metal poor than our full subdwarf population (-1.5 dex). However, the mean metallicity of

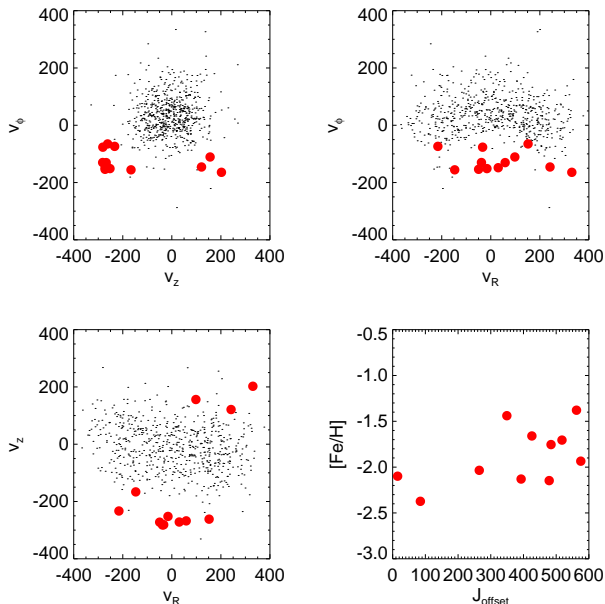


Figure 8. Properties of our H99 stars (see Section 4.2). Upper panels and lower-left panel show the velocity distributions for all stars within 2.5 kpc (small dots) and stars in the H99 region (large circles). The bottom-right panel shows $[\text{Fe}/\text{H}]$ as a function of offset from the centre of the H99 box in the 2D (J_z, J_\perp) plane, which lies at $(-1000, 1950) \text{ kpc km s}^{-1}$.

all 12 stars in the H99 region is -1.8 dex with a dispersion of 0.4 dex, which is comparable to the overall distribution.

The stars in and around the H99 region are illustrated in Fig. 8, which shows their velocities and offset in the (J_z, J_\perp) plane from the centre of the H99 box (the mean error in J_{offset} is $196 \text{ kpc km s}^{-1}$). Given that a smooth halo distribution should give ~ 4 stars in this region, we suspect that not all of these 12 stars are associated with the H99 feature. The distance distribution of these stars is approximately uniform between ~ 1 and ~ 2.5 kpc, with no obvious trend towards smaller distances (unlike K07, who found 67 per cent of their H99 stars were within 1 kpc). However, we note that our sample is biased against $D \lesssim 1$ kpc, as can be seen from Fig. 2, which implies that we could be missing stars from this feature. If we consider the more distant stars with $D > 2.5$ kpc as shown in the lower panel of Fig. 7, we find further potential members of the H99 region. However, these stars appear to come from a more homogeneous background of stars with high angular momentum.

We wish to quantify the prevalence of the H99 stream. We first need to correct for the detection efficiency in order to account for the kinematic bias in our sample. However, the efficiency in Section 2.4 is not directly applicable for stars in the H99 stream, as they do not have the same velocity distribution as the underlying smooth halo. To account for this we re-calculate the efficiency for stars with H99 kinematics. Using this efficiency we predict that up to ~ 7 per cent of all halo stars within 2.5 kpc lie in the H99 box, which is significantly larger than the fraction expected from an entirely smooth halo (~ 1 per cent).

4.3 Retrograde and Prograde Outliers

Various authors have noted the presence of prograde or retrograde outliers when analysing distributions of halo velocities. For example, Venn et al. (2007) identified halo stars on extreme retrograde

orbits ($v_\phi > 200 \text{ km s}^{-1}$) and found them to be significantly more metal poor than typical halo stars. K07 similarly saw an excess of retrograde stars in their halo sample and noted a deficiency in $[\text{Fe}/\text{H}]$ (they found 6 stars with $\langle [\text{Fe}/\text{H}] \rangle = -2.1$ dex). K07 argued that these stars probably belong to a tidally disrupted stream. In addition, K07 found 3 metal-poor stars on extreme prograde orbits, although they postulated that these were more consistent with the underlying halo distribution.

In our sample, we find many stars on extreme orbits, as can be seen from Fig. 7. There are also a number of stars whose angular momenta is sufficiently large for them to lie outside the region of this plot; those stars are listed in Table 5.

However, none of the low J_\perp outliers in Fig 7 look particularly clumped and neither the prograde nor retrograde outliers are significantly in excess of expectations of a smooth distribution. If we analyse stars with $J_\perp < 2000$, then we find 5 stars with $J_z < -2000 \text{ kpc km s}^{-1}$ and 31 stars with $J_z > 2000 \text{ kpc km s}^{-1}$. Our smooth model predicts 2.4 and 30.3 stars in these regions, respectively. Furthermore, neither of these two samples are particularly metal-poor; the mean metallicity is -1.6 dex and -1.4 dex for the prograde and retrograde outliers, respectively. Note that the strong asymmetry in the number of outliers is due to the fact that our detection efficiency is significantly lower for $J_z < 0$.

5 NEW KINEMATIC OVERDENSITIES

There are a number of other possible clumps in our sample. We discuss three of them, which we label Sloan Kinematic Overdensities (SKO), in the following section. The associated stars are given in Table 6.

5.1 SKOa

One interesting feature in the nearby sample shown in the upper-panel of Fig. 7 is the collection of 3 retrograde stars centred on $(J_z, J_\perp) \approx (410, 2420) \text{ kpc km s}^{-1}$. The three stars are all more metal-poor than the halo average, with $\langle [\text{Fe}/\text{H}] \rangle$ of -2.1 dex, and are not clumped spatially (see Table 6). The stars are enclosed by a circular region of the (J_z, J_\perp) plane centred on $(414.8, 2420.3)$ with radius $350 \text{ kpc km s}^{-1}$. Our smooth model predicts that there should be only 0.1 per cent of the sample in this region, which is significantly smaller than the observed fraction of 0.5 per cent. We shall refer to this potential overdensity as SKOa.

When constructing our subdwarf sample, we enforced a strict cut on the quality flags that are raised by the SSPP (see Section 2.2). The SSPP includes two categories of flags: critical and cautionary. For the latter category, it is often possible to determine the stellar parameters, although they should be treated with caution. The vast majority of these stars are flagged because the SSPP pipeline raised issues regarding the $\text{H}\alpha$ line strength (Lee et al. 2008a). In particular, this flag marks stars where ‘there exists a strong mismatch between the strength of the predicted $\text{H}\alpha$ line index, based on the measured $\text{H}\delta$ line index’. If we include stars with cautionary flags into our subdwarf sample, then we gain an additional ~ 700 stars, of which three appear to be associated with the SKOa feature. All of these stars are have similar metallicities to the SKOa members mentioned above (see Table 6).

We plot the velocities of the six SKOa stars in Fig. 9, along with the distribution of $[\text{Fe}/\text{H}]$ as a function of heliocentric distance. Also included in this figure are the stars in a looser selection region with radius $500 \text{ kpc km s}^{-1}$ and with distances up to 5 kpc.

SDSS ID	J_z (kpc km s ⁻¹)	J_\perp (kpc km s ⁻¹)	v_r (km s ⁻¹)	v_ϕ (km s ⁻¹)	v_θ (km s ⁻¹)	Distance (kpc)	[Fe/H] (dex)
SDSS J002012.32+003954.3	3368.9 ± 909.9	1597.8 ± 560.9	365.8 ± 64.7	377.0 ± 98.0	21.0 ± 55.1	4.80 ± 0.52	-1.15 ± 0.12
SDSS J003434.00-011244.6	-3779.3 ± 516.5	1855.1 ± 365.3	-82.2 ± 50.1	-433.8 ± 57.7	-139.6 ± 37.8	3.43 ± 0.33	-1.88 ± 0.13
SDSS J003948.05+003701.5	-135.4 ± 541.0	3119.4 ± 449.6	21.4 ± 53.3	-15.3 ± 61.1	-333.8 ± 46.4	3.43 ± 0.32	-2.56 ± 0.15
SDSS J010450.81-011244.8	-1162.1 ± 270.3	3568.3 ± 303.5	-151.1 ± 33.5	-136.3 ± 32.2	410.8 ± 31.3	1.76 ± 0.20	-1.38 ± 0.11
SDSS J010643.56+005744.2	443.5 ± 801.9	3221.2 ± 812.0	164.0 ± 63.4	45.6 ± 82.0	-301.4 ± 70.9	4.99 ± 0.57	-0.78 ± 0.17
SDSS J010747.56-010447.0	-3240.1 ± 557.3	2043.0 ± 396.2	-124.9 ± 51.3	-356.5 ± 59.6	-180.1 ± 42.7	3.42 ± 0.32	-2.18 ± 0.14
SDSS J013935.21-002545.9	-773.7 ± 420.3	3233.2 ± 428.1	94.3 ± 35.4	-82.2 ± 44.9	-327.5 ± 37.7	3.32 ± 0.38	-1.44 ± 0.11
SDSS J015712.77+011137.1	-929.6 ± 273.1	3748.4 ± 375.6	-112.3 ± 28.1	-103.4 ± 31.0	409.3 ± 35.5	2.01 ± 0.22	-1.35 ± 0.12
SDSS J015755.12+000416.1	661.4 ± 566.9	4171.8 ± 515.7	-4.6 ± 39.2	68.9 ± 58.1	-416.5 ± 43.5	3.30 ± 0.41	-1.43 ± 0.12
SDSS J020359.08-005927.9	-742.4 ± 588.5	3857.5 ± 641.2	-51.4 ± 38.0	-73.1 ± 58.1	355.9 ± 52.6	4.35 ± 0.45	-1.74 ± 0.16
SDSS J021724.92+003127.3	-904.2 ± 541.7	5078.4 ± 704.6	56.8 ± 39.6	-89.4 ± 53.8	-478.2 ± 55.9	3.86 ± 0.42	-1.97 ± 0.12
SDSS J030816.92+011513.3	1956.8 ± 854.4	3322.5 ± 605.5	113.4 ± 29.8	187.7 ± 77.7	306.3 ± 49.8	3.53 ± 0.46	-1.45 ± 0.14

Table 5. Retrograde and Prograde Outliers

SKO	SDSS ID	J_z (kpc km s ⁻¹)	J_\perp (kpc km s ⁻¹)	v_r (km s ⁻¹)	v_ϕ (km s ⁻¹)	v_θ (km s ⁻¹)	Distance (kpc)	[Fe/H] (dex)
a	SDSS J215939.43-004835.6	542.9 ± 347.4	2459.5 ± 262.2	142.4 ± 73.7	71.0 ± 48.6	320.4 ± 57.2	0.94 ± 0.09	-2.07 ± 0.13
a	SDSS J004328.45-001700.0	507.9 ± 700.8	2191.7 ± 353.6	162.8 ± 46.4	60.8 ± 71.6	-258.5 ± 48.9	1.55 ± 0.16	-1.90 ± 0.12
a	SDSS J014424.63+003442.0	193.6 ± 666.6	2609.8 ± 301.1	135.0 ± 26.8	21.7 ± 60.8	-286.9 ± 44.8	2.06 ± 0.19	-2.38 ± 0.13
a*	SDSS J012713.03+011341.8	452.4 ± 850.1	2529.1 ± 375.0	46.8 ± 33.6	53.2 ± 74.3	294.7 ± 50.7	1.29 ± 0.13	-1.90 ± 0.25
a*	SDSS J014332.60-010726.7	397.6 ± 711.3	2281.7 ± 344.3	-212.0 ± 25.6	44.9 ± 65.1	-252.4 ± 39.7	2.01 ± 0.19	-1.76 ± 0.13
a*	SDSS J030435.92-002403.2	51.3 ± 770.0	2233.4 ± 631.6	-217.6 ± 35.4	5.9 ± 68.9	-255.1 ± 56.5	1.08 ± 0.10	-2.06 ± 0.11
b	SDSS J031005.44-001459.4	671.6 ± 797.2	2704.8 ± 774.1	181.8 ± 33.4	61.3 ± 71.3	-236.3 ± 61.7	4.36 ± 0.52	-1.65 ± 0.12
b	SDSS J031049.12+005059.3	997.5 ± 712.7	2490.8 ± 614.4	-25.3 ± 28.4	90.8 ± 62.9	-216.5 ± 49.7	4.33 ± 0.50	-1.30 ± 0.11
b	SDSS J031123.47+001249.6	1305.7 ± 852.2	2698.5 ± 632.5	-189.8 ± 27.2	114.6 ± 71.5	-223.1 ± 49.2	4.95 ± 0.63	-1.57 ± 0.11
b [†]	SDSS J030641.38-002338.0	1221.2 ± 1285.3	3248.5 ± 1198.1	-63.2 ± 42.8	99.9 ± 102.0	-245.5 ± 86.1	6.31 ± 0.85	-1.17 ± 0.11
b [†]	SDSS J030948.29-000111.3	1371.6 ± 1650.7	2433.0 ± 1455.8	15.6 ± 49.7	102.7 ± 121.0	-162.2 ± 108.3	7.87 ± 0.95	-1.61 ± 0.12
b [†]	SDSS J031120.73-000329.4	1655.1 ± 1097.4	2735.3 ± 1050.5	245.6 ± 37.1	141.2 ± 89.6	-216.2 ± 76.9	5.45 ± 0.70	-1.10 ± 0.16
c	SDSS J015840.78-000115.6	1305.3 ± 690.3	2002.9 ± 461.6	-177.6 ± 38.9	130.4 ± 67.5	-183.8 ± 47.4	4.12 ± 0.40	-2.61 ± 0.17
c	SDSS J015840.90+002900.8	1367.9 ± 864.8	2889.3 ± 729.4	87.6 ± 49.5	133.1 ± 82.3	-258.5 ± 62.3	4.60 ± 0.52	-2.61 ± 0.18
c [‡]	SDSS J015806.00+003419.5	1825.3 ± 1378.6	2688.8 ± 1247.4	228.8 ± 62.3	162.2 ± 119.1	-201.9 ± 97.3	6.55 ± 0.82	-2.51 ± 0.12

Table 6. Stars which are candidate members of the three new kinematic overdensities (SKOa-c). Note that the errors on the velocities and angular momenta can be highly correlated; they are included here to give an indication of the relative uncertainties. Notes: * The Sloan Stellar Parameter Pipeline flagged the parameters for these stars as ‘cautionary’ due to issues regarding the H α line strength; [†] The distances for these stars are greater than 5 kpc, which means that the derived velocities are subject to large uncertainties; [‡] The Sloan Stellar Parameter Pipeline flagged the parameters for this star as ‘cautionary’ due to the presence of a strong G-band feature in the spectrum, and the distance is greater than 5 kpc and so the velocities are uncertain.

It seems that a number of the more distant stars may also be associated with this overdensity.

Although the above discussion of SKOa appears tentative, there is striking evidence supporting an accretion scenario for these stars. In Fig. 12, we overplot the locations of globular clusters using data from Dinescu, Girard & van Altena (1999) on our distribution of kinematic overdensities in the (J_z , J_\perp) plane. We immediately see the clump of four clusters standing out around SKOa. These clusters are NGC5466, NGC6934, NGC7089/M2 and NGC6205/M13, which have metallicity -2.22, -1.54, -1.58 and -1.65 dex, respectively. Of these four clusters, NGC5466 is known to be disrupting (Odenkirchen & Grebel 2004; Belokurov et al. 2006) and its orbit takes it to within a few kpc of the solar neighbourhood (Fellhauer, private communication; see also Fellhauer et al. 2007). This, along with the fact that the SKOa stars have similarly low metallicity, indicates that they could well be tidal debris from NGC5466. However, the fact that there are four clusters located in the same region of the (J_z , J_\perp) plane raises the intriguing possibility that all could be

associated to a single major accretion event. Previous authors have questioned whether subsets of these four clusters may be associated (e.g. Dinescu, Girard & van Altena 1999; Palma, Majewski & Johnston 2002; Mackey & Gilmore 2004), but it appears that no one to date has attempted to explicitly associate all four clusters.

The uncertainties on the velocities of these clusters varies; NGC6205 and NGC7089 have reasonably well constrained angular momenta (with error on J_z and J_\perp of between 200 and 400 kpc km s⁻¹), while for NGC5466 and NGC6934 this is less well constrained (with error of between 400 and 900 kpc km s⁻¹). This is due to the uncertainties in the proper motion combined with the large distances to these two clusters (~7 to ~15 kpc). However, although the error for NGC5466 seems large, its proper motion is confirmed by Fellhauer et al. (2007) and so its location in the (J_z , J_\perp) plane is robust.

Note that a similar retrograde feature has been identified by Dinescu (2002, see also Brook et al. 2003) from the sample of Chiba & Beers (2000). This feature, which they postulated could

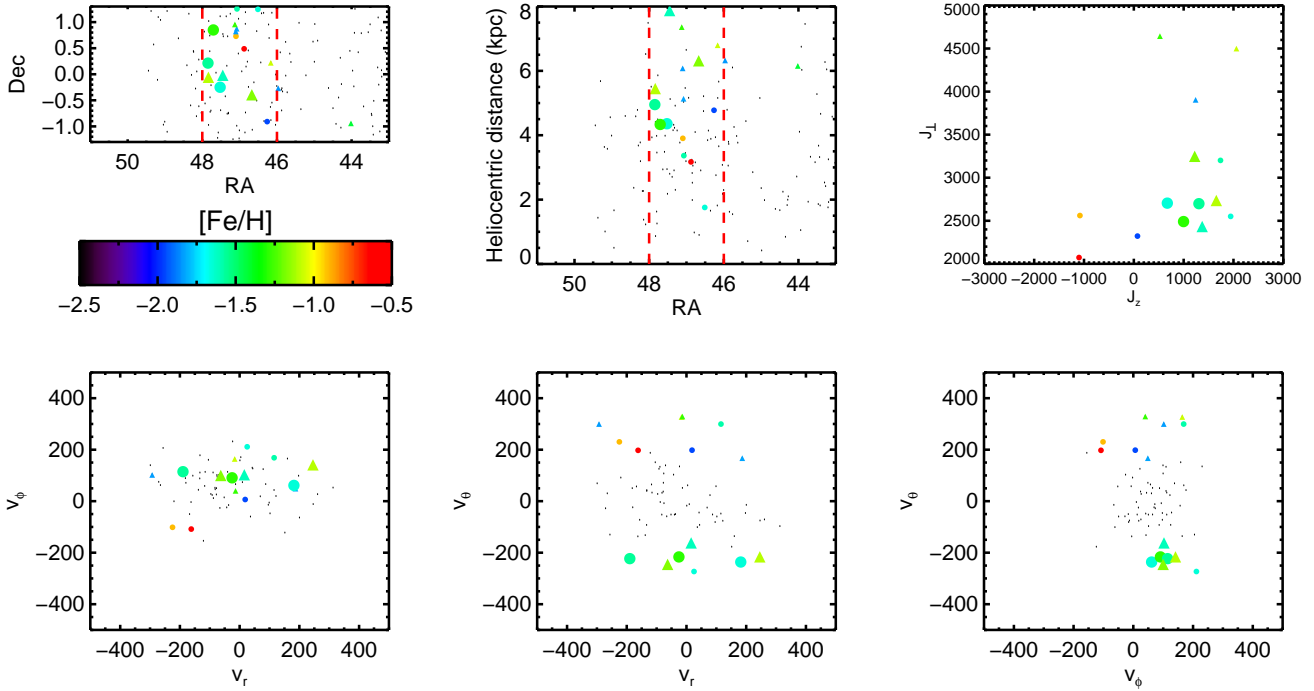


Figure 10. Properties of the SKOb overdensity (see Section 5.2 and Table 6). The coloured symbols denote stars with $J_{\perp} > 2000 \text{ kpc km s}^{-1}$ and are colour-coded according to metallicity, with SKOb members (large symbols) differentiated from other high- J_{\perp} stars (small symbols). The triangles denote stars with $D > 5 \text{ kpc}$, which have larger uncertainties in their kinematics. We also show stars with $J_{\perp} < 2000 \text{ kpc km s}^{-1}$ for comparison (small points). The vertical dashed lines denote the right ascension range $46^{\circ} < \alpha < 48^{\circ}$. Note the lack of high- J_{\perp} stars outside of this range.

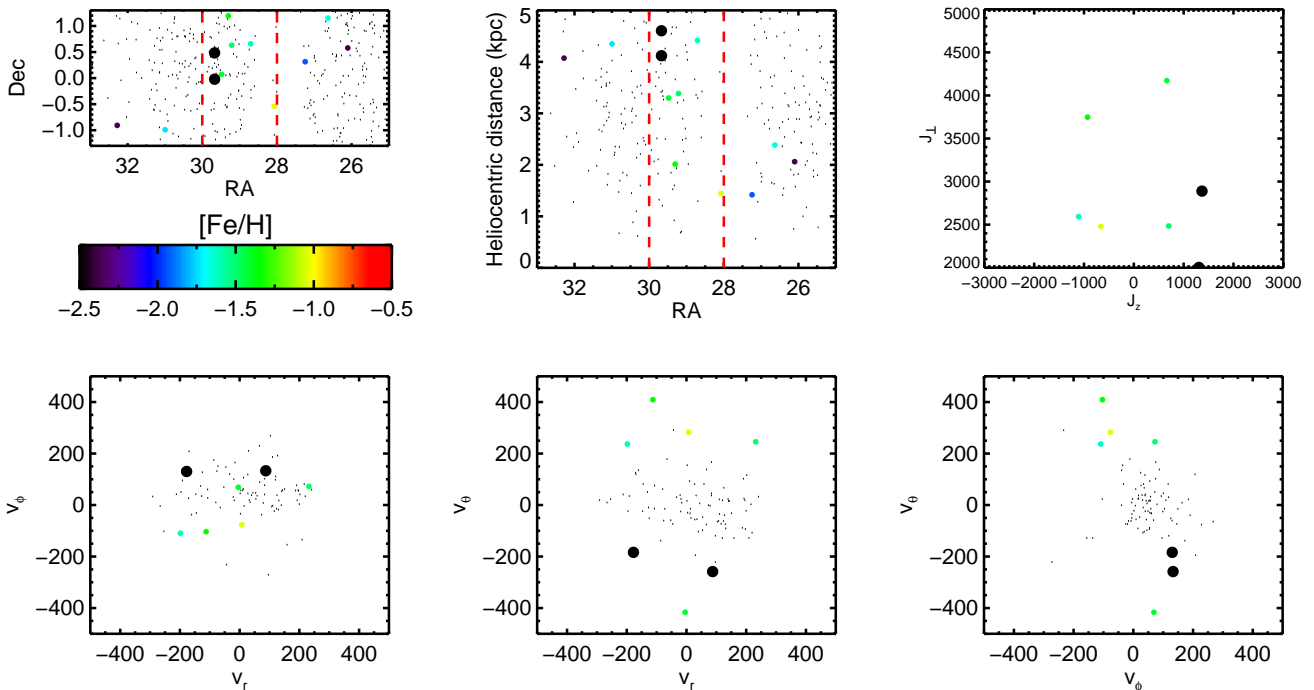


Figure 11. Properties of SKOc sample stars in the range $28^{\circ} < \alpha < 30^{\circ}$ (see Section 5.2 and Table 6). The upper-middle and upper-left panels also show stars outside this α range for comparison. The coloured symbols denote stars with $J_{\perp} > 2000 \text{ kpc km s}^{-1}$ and are colour-coded according to metallicity, with the two metal-poor SKOc members (large symbols) differentiated from other high- J_{\perp} stars (small symbols).

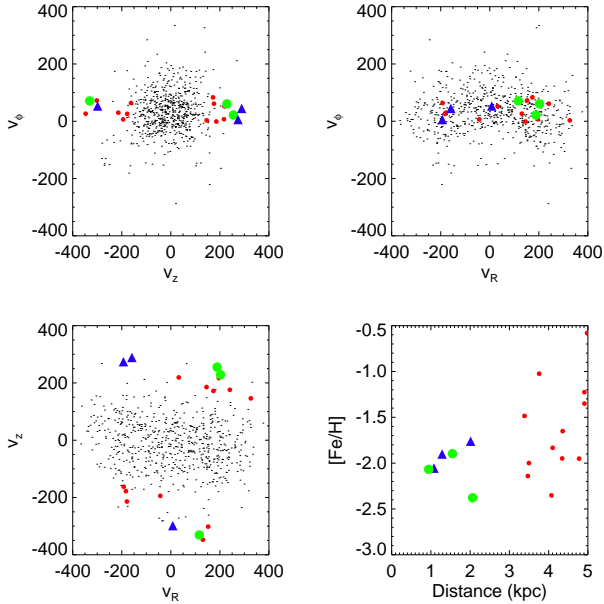


Figure 9. Properties of the SKOa overdensity (see Section 5.1 and Table 6). The upper two panels and lower left panel show the velocity distributions for all stars within 2.5 kpc of the Sun (small points), members of the SKOa overdensity (large circles), additional members with cautionary SSPP flags (triangles), and potential members with distance greater than 2.5 kpc (small circles). The members with $D < 2.5$ kpc are enclosed within a $350 \text{ kpc km s}^{-1}$ circle centred on $(413.6, 2419.9) \text{ kpc km s}^{-1}$, while the potential members with $2.5 < D < 5$ kpc are enclosed within a larger radius ($500 \text{ kpc km s}^{-1}$). The bottom right panel shows $[\text{Fe}/\text{H}]$ as a function of heliocentric distance for stars with offset in the 2D (J_z, J_\perp) plane less than $500 \text{ kpc km s}^{-1}$ from the centre of the SKOa clump.

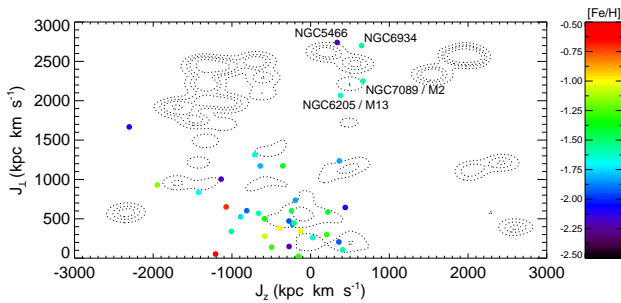


Figure 12. Angular momentum distribution of the 38 globular clusters from Dinescu, Girard & van Altena (1999) with 6D phase-space, where the colour corresponds to cluster metallicity. Contours denote the kinematic overdensities for halo stars within 2.5 kpc (see Section 4), corresponding to 1, 3, 5 and 10 sigma significance. Note the four globular clusters potentially associated to the overdensity at $(J_z, J_\perp) \approx (500, 2500) \text{ kpc km s}^{-1}$; these are NGC5466, NGC6934, NGC7089/M2, NGC6205/M13. In this coordinate system the Sun would lie at approximately $(-1800, 0) \text{ kpc km s}^{-1}$.

be debris torn from the system that once contained ω Centauri, was observed as an excess of stars with small retrograde velocities. However, as can be seen by comparing our Fig. 9 to fig. 15 of Chiba & Beers (2000), the stars in our SKOa feature are not compatible. Although our stars indeed have small retrograde velocities, the J_\perp

velocities of Chiba & Beers (2000) are significantly smaller than ours and no more than one of their stars lies in our SKOa region.

5.2 SKOb, SKOc

It is clear from Fig. 7 that there are a significant number of more distant stars ($2.5 < D < 5$ kpc) with large values of J_\perp . To establish whether these stars are clumped, we must investigate their spatial distribution along the stripe. As our sampling is very inhomogeneous, we are actually interested in identifying locations on the stripe where the fraction of high J_\perp objects is anomalous, rather than the absolute number.

Since our field of view consists of a narrow 2.5° wide stripe at constant declination, streams will typically cut through the stripe and be localised in right ascension α . Therefore, we analyse our data by looking at 2° sections in α along the stripe, concentrating only on bins which contain more than 30 subdwarfs. We calculate the fraction of stars in a bin with $J_\perp > 2000 \text{ kpc km s}^{-1}$ (considering all stars with $D < 5$ kpc), and also the expected fraction as predicted from our smooth model. When we carry out the calculation of the binomial probability, we take into account the fact that there are 21 bins with more than 30 stars, i.e. we determine the probability that any of these 21 bins has the observed fraction of high J_\perp stars. The smooth model predicts a factor of ~ 1.9 fewer high J_\perp stars in total compared to the observed fraction ($60/1717$). This indicates the presence of non-Gaussian tails in the velocity distributions and it is these outliers that could harbour potential accretion remnants.

There are two locations on the stripe where the binomial probability of obtaining the observed fraction of high J_\perp stars is less than ~ 0.05 and for which there are more than three such stars. We call these two clumps SKOb and SKOc. Candidate members of these overdensities are given in Table 6.

The clump SKOb is located in the range $46^\circ < \alpha < 48^\circ$, where we find 8 of 57 stars have $J_\perp > 2000 \text{ kpc km s}^{-1}$. Our smooth model predicts that we should see only 2.1 stars and the corresponding binomial probability is 0.03. Various properties of the SKOb stars are shown in Fig. 10, from which we see that there are a significant number of stars in this α range at distances between 3 and 5 kpc. It is intriguing to note that most of these objects have retrograde velocities ($J_z > 0$). There is a clear clump of three stars located in a small region of the (v_ϕ, v_θ) plane² around $(89, -225) \text{ km s}^{-1}$. Furthermore, these three stars have similar metallicities ($\langle [\text{Fe}/\text{H}] \rangle = -1.5$ dex) and distances (see Table 6). Given that these stars are close to our limiting distance of 5 kpc, it is worth looking at those stars which lie outside this distance cut. So in Fig. 10, we also include stars in this α range with distances up to 8 kpc. Although their velocities are less certain, there are sufficient stars to warrant their inclusion. Clearly, these more distant stars reinforce the significance of the potential overdensity. The clump in the (v_ϕ, v_θ) plane is even more pronounced, with six stars now lying in this region. All six stars are located in a loose clump in the (J_z, J_\perp) plane, with $J_z \in (670, 1660) \text{ kpc km s}^{-1}$ and $J_\perp \in (2430, 3250) \text{ kpc km s}^{-1}$. Note that these additional three stars also have similar metallicities to those with $D < 5$ kpc. If we loosen

² Note that if these stars were debris from an accreted satellite, one might naively expect them to also have the same values of v_r . However, as can be seen from the modelling of satellite disruption for the H99 stream, this is not necessarily the case; although the model presented in Képley et al. (2007) is localised in (v_z, v_ϕ) -space, it has an extended v_r distribution.

the cut on the SSPP flag as above (see Section 5.1), then we do not gain any additional potential members for this overdensity.

The second clump, SKOc, is located at $28^\circ < \alpha < 30^\circ$ and has 7 of 69 stars with $J_\perp > 2000$ kpc km s⁻¹. The smooth model predicts only 1.9 stars (with corresponding binomial probability of 0.07). The properties of these stars are illustrated in Fig. 11. Unlike SKOb, there is no obvious clumping in velocity space. However, of note is the pair of two metal-poor stars which lie at very similar distances ($D \approx 4.1, 4.6$ kpc, $[\text{Fe}/\text{H}] \approx -2.6, -2.6$ dex) and are relatively close to each other on the sky (separated by half a degree). These two stars are located in close proximity in the (v_ϕ, v_θ) plane, but their angular momenta are not particularly close ($J_\perp \approx 2000 \pm 460, 2890 \pm 730$ kpc km s⁻¹). This means that the chance of these two stars belonging to a kinematic overdensity is perhaps unlikely. Despite this, their case is strengthened to some extent when we include stars with less secure parameters; there is one additional metal-poor star located in the (v_ϕ, v_θ) plane at $(162, -202)$ km s⁻¹ with $D \approx 6.6$ kpc and $[\text{Fe}/\text{H}] \approx -2.5$ dex. As well as being more distant than our standard cut of 5 kpc, there is also a cautionary flag raised in the SSPP. The flag records that the star may be exhibiting a strong CH *G*-band (around 4300 Å) relative to what is expected for a ‘normal’ star (Lee et al. 2008a) and implies that the spectral parameters should be treated with caution. It lies very close on the sky to the pair of metal-poor stars previously mentioned, but given the various uncertainties it is far from clear whether we can claim that it is associated to the pair of metal-poor stars in this region. Therefore, in conclusion, the validity of this feature is rather tentative and it could simply illustrate that we have reached the limits of this method.

6 CONCLUSIONS

This paper has presented a catalogue of ~ 1700 halo subdwarfs within a heliocentric distance of ~ 5 kpc. Our analysis is restricted to a particular patch of sky, Stripe 82 of the Sloan Digital Sky Survey (SDSS), and exploits the light-motion curve catalogue constructed by Bramich et al. (2008). The exceptional precision of the SDSS photometry allows us to determine distances with an uncertainty of ~ 10 per cent from a photometric parallax relation. As a consequence, we obtain high-quality tangential velocities (with typical errors of $30 - 50$ km s⁻¹) using the proper motions derived from the light-motion curves. Radial velocities are obtained from SDSS spectra. So, this sample of halo stars has full six-dimensional phase-space information, allowing us to probe in detail the kinematical structure of the stellar halo. As our data are restricted to Stripe 82, we may be susceptible to spatial variations present in the halo population. However, even if the halo population is not well-mixed, our ~ 250 square degree field-of-view is sufficiently large to overcome any small-scale effects.

The size of our sample allows us to determine the orientation and semi-axes of the velocity ellipsoid of the stellar halo to excellent accuracy. The velocity ellipsoid is almost precisely aligned in the spherical polar coordinate system, indicating that the total potential must be nearly spherical (Smith, Evans & An 2009). The velocity dispersions are $(\sigma_r, \sigma_\phi, \sigma_\theta) = (143 \pm 2, 82 \pm 2, 77 \pm 2)$ km s⁻¹. The values of the dispersions are significantly smaller than previous estimates, although the ratios of the dispersions are in good agreement. A simple distribution function that matches the kinematic data is constructed – and it suggests that the density of the stellar halo is only mildly flattened and falls off with distance like $\rho \sim r^{-3.8}$.

The stellar halo exhibits no net rotation. The velocity dispersions are reasonably well fit by a Gaussians, with the exception of the v_ϕ component which is asymmetric. We believe that this is a real effect. It appears to be more pronounced for metal rich stars in our sample. None of the kinematic substructures are able to account for this asymmetry.

On the issue of substructure, we confirm the presence of the stream identified by Helmi et al. (1999). Using the angular momentum components (J_z, J_\perp) , we find a number of other potential substructures, which we label Sloan Kinematic Overdensities (SKOs). Two of these new features are particularly striking, containing a number of stars that are localised in both kinematics and metallicity. The metal-poor overdensity SKOa ($[\text{Fe}/\text{H}] \approx -2.1$ dex) appears to be coincident in the (J_z, J_\perp) plane with an association of four globular clusters (NGC5466, NGC6934, NGC7089/M2 and NGC6205/M13), suggesting that they may have been part of the same accretion event. If so, then this implies that the progenitor must have been a large satellite, similar in size to Fornax. We are currently investigating the orbits of these stars and clusters and plan to test this hypothesis using simulations.

ACKNOWLEDGMENTS

The authors wish to thank Mario Jurić, Matthew G. Walker and an anonymous referee for advice and guidance, as well as Jeff Munn and Łukasz Wyrzykowski for help with the Light-Motion Curve Catalogue. MCS acknowledges support from the STFC-funded ‘Galaxy Formation and Evolution’ program at the Institute of Astronomy, University of Cambridge.

Funding for the SDSS and SDSS-II has been provided by the Alfred P. Sloan Foundation, the Participating Institutions, the National Science Foundation, the U.S. Department of Energy, the National Aeronautics and Space Administration, the Japanese Monbukagakusho, the Max Planck Society, and the Higher Education Funding Council for England. The SDSS Web Site is <http://www.sdss.org/>.

The SDSS is managed by the Astrophysical Research Consortium for the Participating Institutions. The Participating Institutions are the American Museum of Natural History, Astrophysical Institute Potsdam, University of Basel, Cambridge University, Case Western Reserve University, University of Chicago, Drexel University, Fermilab, the Institute for Advanced Study, the Japan Participation Group, Johns Hopkins University, the Joint Institute for Nuclear Astrophysics, the Kavli Institute for Particle Astrophysics and Cosmology, the Korean Scientist Group, the Chinese Academy of Sciences (LAMOST), Los Alamos National Laboratory, the Max-Planck-Institute for Astronomy (MPIA), the Max-Planck-Institute for Astrophysics (MPA), New Mexico State University, Ohio State University, University of Pittsburgh, University of Portsmouth, Princeton University, the United States Naval Observatory, and the University of Washington.

REFERENCES

- Abazajian K. et al., 2009, ApJS, 182, 543
- Allende Prieto C., Beers T.C., Wilhelm R., Newberg H.J., Rockosi C.M., Yanny B., Lee Y.S., 2006, ApJ, 636, 804
- Allende Prieto C. et al., 2008, AJ, 136, 2070
- Arnold R., & Gilmore G. 1992, MNRAS, 257, 225

- Binney J., Tremaine S., 1987, *Galactic Dynamics*, Princeton University Press
- Belokurov V., Evans N.W., Irwin M.J., Hewett P.C., Wilkinson M.I., 2006, *ApJ*, 637, L29
- Belokurov V., et al. 2007, *ApJ*, 657, L89
- Bramich D.M. et al., 2008, *MNRAS*, 386, 887
- Brook C.B., Kawata D., Gibson B.K., Flynn C., 2003, *ApJ*, 585, L125
- Carollo D. et al., 2007, *Nature*, 450, 1020
- Chiba M., Beers T.C., 2000, *AJ*, 119, 2843
- Clewley L., Warren S. J., Hewett P. C., Norris J. E., Wilkinson M. I., & Evans N. W. 2005, *MNRAS*, 362, 349
- de Zeeuw P. T., Evans N. W., & Schwarzschild M. 1996, *MNRAS*, 280, 903
- Dinescu D.I., 2002, in van Leeuwen F., Hughes J. D., Piotto G., eds, *ASP Conf. Ser. Vol. 265, Omega Centauri: A Unique Window into Astrophysics*. Astron. Soc. Pac., San Francisco, p.365
- Dotter A., Chaboyer B., Jevremović D., Kostov V., Baron, E., Ferguson, Jason W., 2008, *ApJS*, 178, 89
- Dinescu D.I., Girard T.M., van Altena W.F., 1999, *AJ*, 117, 1792
- Dehnen W., Binney J.J., 1998, *MNRAS*, 298, 387
- Eisenstein D.J. et al., 2006, *ApJS*, 167, 40
- Fellhauer M., et al. 2006, *ApJ*, 651, 167
- Fellhauer M., Evans N.W., Belokurov V., Wilkinson M.I., Gilmore G., 2007, *MNRAS*, 380, 749
- Freeman K. C. 1987, *ARAA*, 25, 603
- Girard T.M., Korchagin V.I., Casetti-Dinescu D.I., van Altena W.F., López C.E., Monet D.G., *AJ*, 132, 1768
- Gould A., 2003a, *ApJ*, 583, 765 (Erratum: 2004, *ApJ*, 607, 653)
- Gould A., 2003b, *ApJ*, 592, L63
- Gould A., 2007, *arXiv:0804.2448*
- Gould A., Popowski P., 1998, *ApJ*, 508, 844
- Helmi A., White S.D.M., de Zeeuw P.T., Zhao H., 1999, *Nature*, 402, 53 (H99)
- Ibata R. A., Gilmore G., & Irwin M. J. 1994, *Nature*, 370, 194
- Ibata R. A., Gilmore G., & Irwin M. J. 1995, *MNRAS*, 277, 781
- Ivezić Ž., et al. 2008, *ApJ*, 684, 287
- Jurić M. et al., 2008, *ApJ*, 673, 864
- Kepley A.A. et al., 2007, *AJ*, 134, 1579
- Lee Y. S. et al., 2008a, *AJ*, 136, 2022
- Lee Y. S. et al., 2008b, *AJ*, 136, 2050
- Majewski S.R., 1992, *ApJS*, 78, 87
- Mackey A.D., Gilmore, G.F., 2004, *MNRAS*, 355, 504
- Mihalas D., Binney J. 1981, *Galactic Astronomy* (2nd ed.), W. H. Freeman and Co, San Francisco
- Monet D. G., et al. 2003, *AJ*, 125, 984
- Morrison H. L., et al. 2009, *ApJ*, 694, 130
- Munn J. A., et al. 2004, *AJ*, 127, 3034
- Newberg H. J., et al. 2002, *ApJ*, 569, 245
- Odenkirchen M., Grebel E.K., 2004, in Prada F., Martinez Delgado D., Mahoney T.J., eds, *ASP Conf. Ser. Vol. 327, Satellites and Tidal Streams*. Astron. Soc. Pac., San Francisco, p. 284
- Norris J., 1986, *ApJS*, 61, 667
- Palma C., Majewski S.R., Johnston K.V., 2002, *ApJ*, 564, 736
- Reid I.N., van Wyk F., Marang F, Roberts G., Kilkenny D., Mahoney S., 2001, *MNRAS*, 325, 931
- Schlegel D.J., Finkbeiner D.P., Davis M., 1998, *ApJ*, 500, 525
- Sesar B., Ivezić Ž, Jurić M., 2008, *ApJ*, 689, 1244
- Smith M.C. et al., 2007, *MNRAS*, 379, 755
- Smith M.C., Evans N.W., An J., 2009, *ApJ*, 698, 1110
- Soubiran C., Bienaymé O., Siebert A., 2003, *A&A*, 398, 141
- Venn K.A., Irwin M., Shetrone M.D., Tout C.A., Hill V., Tolstoy E., 2004, *AJ*, 128, 1177
- Woolley R., 1978, *MNRAS*, 184, 311
- Yanny B., et al. 2003, *ApJ*, 588, 824
- Yanny B., et al. 2009, *AJ*, in press (arXiv:0902.1781)
- York D. G., et al. 2000, *AJ*, 120, 1579
- Watkins L., et al. 2009, *MNRAS*, in press (arXiv:0906.0498)
- White S. D. M. 1985, *ApJ*, 294, L99

APPENDIX A: POTENTIAL CONTAMINANTS

There are three main sources of contamination: white dwarfs, disc dwarfs and background giants. We discuss each in turn and conclude that our contamination level is less than ~ 1 per cent.

A1 White dwarfs

In a RPM diagram, the white dwarfs are fainter and bluer than the halo subdwarfs. Their presence in Fig. 1 is only just discernible as the cloud around $((g-i), H_r) \approx (-0.4, 17)$. Although the density of white dwarfs in this figure is clearly small, it is possible that white dwarfs with small proper motions enter our subdwarf region. As stated in Section 2.2, we require that the SSPP flag is set to ‘nnnn’. This flag includes a check for candidate white dwarfs (Lee et al. 2008a) and so our sample should be free from such contamination.

As a check, we cross-matched our subdwarf sample with the catalogue of spectroscopically confirmed white dwarfs from the fourth data release (DR4) of the SDSS (Eisenstein et al. 2006). This catalogue was constructed via both automated criteria and visual inspection and so should be reasonably complete. We find that none of their white dwarfs overlap with our subdwarf sample. Although the Eisenstein et al. (2006) catalogue contains only DR4 data, we know that ~ 60 per cent of our subdwarf spectra were included in DR4 and so, assuming the fraction of white dwarfs does not vary with SDSS data releases, we can expect $\lesssim 1$ white dwarf to contaminate our subdwarf sample.

A2 Disc dwarfs

Although our RPM cut in Section 2.1 rejects stars with kinematics similar to the Sun (hence retaining mainly fast moving halo stars), it is possible that some disc stars could enter our sample. Contamination by thin-disc stars is negligible due to two factors. First, the small scale-height (~ 200 pc) of the thin disc means that our sample, which goes out to a few kpc below the plane, should have minimal contamination. Second, the thin disc is cold so that it is highly unlikely that a thin disc star would have large enough proper motion to pass our RPM cut. However, it is possible that there may be some contamination from the hotter thick-disc component. Previous studies based on similar RPM cuts have found levels of disc contamination to be of order two per cent (Gould 2007).

To quantify the contamination from disc dwarfs in our sample we analyse the kinematics of the stars. We calculate the probability that a star belong to a particular population (i.e. thin disc, thick disc or halo) by comparing its velocity to a toy model constructed using Gaussian distributions for each component of the velocity, taking into account the different scale-heights and local density normalisations. For the scale-heights and disc kinematics we follow Smith et al. (2007), with the exception of the mean rotation velocity of the thick disc which we model using the parameters

determined from Girard (2006), i.e. $v_\phi = -195 + 30|z|$ km s⁻¹. We model the halo component using the kinematics of Képley et al. (2007) and assume that the halo density does not vary significantly within the volume probed. As expected, we find that none of our stars are compatible with the thin disc. For the thick disc we analyse the stars with $[\text{Fe}/\text{H}] > -1.5$ dex, since this is the three-sigma lower limit on the thick-disc metallicity according to Soubiran et al. (2003). Although there are no stars in this $[\text{Fe}/\text{H}]$ range with thick-disc membership probabilities of greater than 0.36, there are six stars with probabilities of between 0.2 and 0.36. If we add up the thick-disc probabilities of all stars in this $[\text{Fe}/\text{H}]$ range we can estimate the total level of contamination. Note that this will probably be an overestimate because the kinematics of the thick disc overlap those of the halo, which implies that even a pure halo sample will be estimated to have a non-zero level of contamination. Using this technique we estimate that the thick-disc contamination should be no more than 10.2 stars, i.e. less than one per cent. This should have little bearing on our results. As a test we repeated the analysis of Section 3 using only stars at distances of more than 2.5 kpc from the Galactic plane and found that global kinematic properties were unchanged.

A3 Background Giants

Another possible source of contamination is from faint background giants. However, given the RPM cut, we see that a star must have a sufficiently high μ to shift it into the subdwarf regime. For example, a stationary distant star with $r = 19$ mag and a spurious $\mu = 4$ mas yr⁻¹ would have $H_r = 12$ mag. If the star was blue enough then it could conceivably pass the H_r cut. However, in our final subdwarf sample we find that the star with the least significant proper motion is inconsistent with $\mu = 0$ at the 2.5σ level, which means contamination from distant (and hence stationary) stars is negligible.

APPENDIX B: TURN-OFF CORRECTION FOR PHOTOMETRIC PARALLAX RELATION

We estimate distances using a photometric parallax relation based on Ivezić et al. (2008), who construct a relation using data from a number of globular clusters. They first determine a $(g-i) - M_r$ colour-magnitude sequence for stars on the main-sequence by identifying the colour of the main-sequence turn-off for these clusters (i.e. the point at which the slope of the colour-magnitude relation becomes vertical) and discarding all data within 0.05 mag of the turn-off. Once they have this relation, they then devise a correction to account for the presence of the main-sequence turn-off, which they base on the sequence for the cluster M13.

However, the morphology of the colour-magnitude relation around the turn-off region will clearly be dependent on both metallicity and age, and so we would like to construct a correction which incorporates these effects. In order to do this, we use the stellar models of Dotter et al. (2008), taking isochrones with ages from 1 to 15 Gyr (in steps of 0.5 Gyr) and $[\text{Fe}/\text{H}]$ from -0.5 to -2.5 (in steps of 0.5 dex). Following the compilation of Venn et al. (2007) we choose $[\alpha/\text{Fe}] = 0.3$, which is representative for our halo $[\text{Fe}/\text{H}]$ range.

We take each set of isochrones and, in the same manner as Ivezić et al. (2008), we shift each sequence so that it has $M_r = 0$ for $(g-i) = 0.6$. Then, for a given $[\text{Fe}/\text{H}]$, we calculate mean M_r as a function of $(g-i)$ in the range $0.3 < (g-i) < 0.6$, considering only

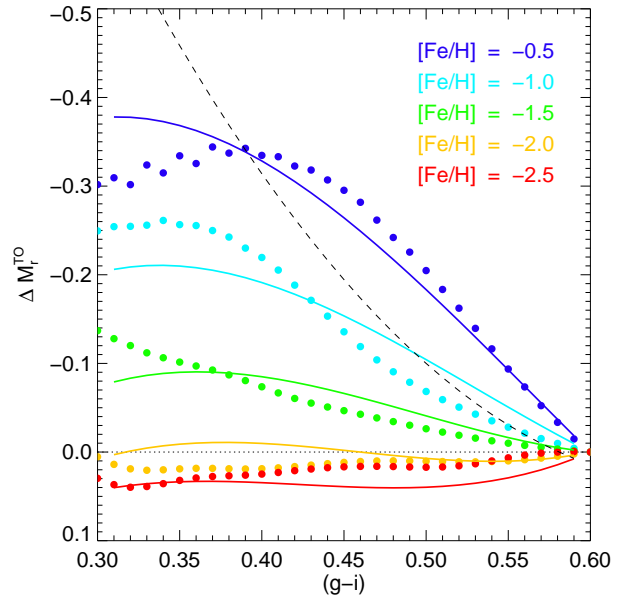


Figure B1. Our correction to the photometric parallax relation due to the main-sequence turn-off. The points denote mean magnitudes from the stellar models and the corresponding solid curves denote the polynomial fit given in equation B1, with $[\text{Fe}/\text{H}]$ increasing from -2.5 (bottom line) to -0.5 (top line). The dashed line corresponds to the turn-off correction of Ivezić et al. (2008).

model data up to the main-sequence turn-off. Since we know the approximate age distribution of the halo population, we calculate a weighted mean using a Gaussian prior with mean and sigma of 10 and 2 Gyr, respectively.³ We then calculate the offset between the mean model magnitude and the uncorrected relation of Ivezić et al. (2008), i.e. that given in equations (A1-A5). This is shown in Fig. B1, where the effect of the turn-off correction is to increase the brightness of stars compared to the uncorrected relation.

This data is then fit with a third-order polynomial, resulting in the following equation which is applicable for stars in the range $0.3 < (g-i) < 0.6$ and $-2.5 < [\text{Fe}/\text{H}] < -0.5$,

$$\Delta M_r^{\text{TO}} = a_0 x + a_1 x y + a_2 x^3 + a_3 x^2 y + a_4 x y^2, \quad (\text{B1})$$

where $x = (g-i) - 0.6$, $y = [\text{Fe}/\text{H}]$, and $a_0 = 2.87$, $a_1 = 2.25$, $a_2 = -9.79$, $a_3 = 2.07$, $a_4 = 0.31$. Note that we do not include terms depending solely on y since we require the relation to go through $\Delta M_r^{\text{TO}} = 0$ for $(g-i) = 0.6$. We also discard the x^2 term since this has no effect on the fit. Although the fit is far from perfect, given the overall uncertainties in the method we believe this should provide a reasonable approximation.

In order to avoid any divergent behaviour in this relation we do not extrapolate equation (B1) beyond $[\text{Fe}/\text{H}] = (-2.5, -0.5)$. For stars with metallicities outside this range, we use the relation at the limit of our allowed range (i.e. -2.5 dex for the metal-poor stars and -0.5 dex for the metal-rich stars). This has very little bearing on our results: although we have around 30 stars with $0.3 < (g-i) < 0.6$ and $[\text{Fe}/\text{H}] < -2.5$, the relation converges at the metal-poor end and so the $[\text{Fe}/\text{H}] = -2.5$ relation should provide a good approximation;

³ One could also incorporate a prior based on the initial mass function or, equivalently, the luminosity function. However, we investigated this and found it had a negligible effect on our results.

from Fig. B1 it can be seen that the relation does not converge at the metal-rich end, but this is of little consequence since there are fewer than 10 stars with $0.3 < (g-i) < 0.6$ and $[\text{Fe}/\text{H}] > -0.5$.

Clearly the uncertainties on the parallax relation will be larger in this colour range due to the scatter in this turn-off correction. To estimate the uncertainty, we calculate the standard deviation in M_r when we calculate the mean. The scatter varies as a function of colour and metallicity, but if we take the relation with the largest scatter (corresponding to $[\text{Fe}/\text{H}] = -0.5$ dex) we find the following relation,

$$\delta(\Delta M_r^{TO}) = 0.39 - 0.65(g-i). \quad (\text{B2})$$

When estimating distances for our stars we add this uncertainty in quadrature to the other sources of error.